

# Characterizing Disproportionate Permeability Reduction Using Synchrotron X-Ray Computed Microtomography

R.S. Seright, SPE, New Mexico Petroleum Recovery Research Center; J. Liang, SPE, Idaho Natl. Engineering and Environmental Laboratory; W. Brent Lindquist, SPE, State U. of New York at Stony Brook; and John H. Dunsmuir, ExxonMobil Research & Engineering Co.

## Summary

X-ray computed microtomography was used to investigate why gels reduce permeability to water more than that to oil in strongly water-wet Berea sandstone and in an oil-wet porous polyethylene core. Although the two porous media had very different porosities (22% vs. 40%), the distributions of pore sizes and aspect ratios were similar. A Cr(III)-acetate-HPAM gel caused comparable oil and water permeability reductions in both porous media. In both cores, the gel reduced permeability to water by a factor 80 to 90 times more than that to oil. However, the distributions of water and oil saturations (vs. pore size) were substantially different before, during, and after gel placement. This paper examines the mechanism for the disproportionate permeability reduction in the two porous media.

## Introduction

Many polymers and gels can reduce the permeability to water more than that to oil or gas.<sup>1-15</sup> This property is critical to the success of water-shutoff treatments in production wells if hydrocarbon-productive zones cannot be protected during polymer or gelant placement.<sup>2,3</sup> However, the magnitude of the effect has been unpredictable from one application to the next. Presumably, the effect would be more predictable and controllable if we understood why the phenomenon occurs. Although many mechanisms have been considered (see **Table 1**), the underlying cause of the disproportionate permeability reduction remains elusive.

Previously, we used NMR imaging to observe disproportionate permeability reduction on a microscopic scale.<sup>16</sup> Results from these experiments revealed that the imaging technique had many limitations that prevented us from obtaining reliable pore-level images. Most importantly, the spatial resolution was on the order of hundreds of micrometers, which was too low to clearly distinguish fluid pathways on the pore level.

In this paper, we describe imaging experiments using high-resolution computed X-ray microtomography (XMT) to compare the oil and water pathways and fluid distributions before and after gel treatment. The current generation of synchrotron-based XMT scanners provides the ability to obtain 3D pore-level images of rock samples with a spatial resolution on the order of micrometers.<sup>17-23</sup> For this study, we used the ExxonMobil beamline X2-B at the Natl. Synchrotron Light Source.<sup>18</sup> X2-B is a dedicated XMT imaging facility capable of producing continuous registered stacks of  $2,048 \times 2,048 \times 1,024$  14-bit 3D images of X-ray linear attenuation coefficients at energies tunable from 8 to 40 keV. The highly collimated synchrotron X-rays permit the reconstruction of a 3D image from 2D projections taken at uniformly spaced angles between 0 and 180°. X2-B converts the pattern X-rays transmitted by the specimen (projections) to a visible light image with a thin single crystal of CsI(Na). This image was magnified by an optical microscope objective onto a  $1,024 \times 1,024$  charge coupled device

(CCD). Using Fourier methods, the set of angular projections at each row of pixels in the CCD was used to reconstruct the cross-sectional slice at that row. These slices were stacked to form the 3D image. In this work, a  $5\times$  microscope objective was used to provide a pixel size of  $4.1 \mu\text{m}$  and a 4.1-mm field of view. Because part of the core was outside the imaged area, a profile extension method was used to suppress edge artifacts.

Several authors used XMT to characterize the microscopic structure of porous media.<sup>17,19,23</sup> For a 15-darcy sandstone, Coles *et al.*<sup>19</sup> found a mean tortuosity of 2.7, with a range from 1.5 to 4.5. Along a 2.2-mm-long section of this core, porosity varied only a few percent around the average value (26.4%). After oilflooding, this core was waterflooded to a water saturation of 25.1%. Interestingly, large variations in water saturation were observed along the 2.2-mm-long section, ranging from 12 to 39%. A 3D view showed the nonwetting phase (water, in this case) to exist as large ganglia (blobs of nonwetting phase that extend over multiple pores, often exhibiting a branched structure).<sup>19</sup>

Chatzis *et al.*<sup>24,25</sup> suggested that rock heterogeneity can be responsible for saturation variations within a porous medium. Nonwetting phase saturations that are lower than expected can occur when clusters of small pores are dispersed in a matrix dominated by large pores. In contrast, nonwetting phase saturations that are higher than expected can occur when clusters of large pores are dispersed in a matrix dominated by small pores.<sup>24</sup> However, significant saturation variations can occur even in homogeneous porous media, depending on the pore-body/pore-throat aspect ratio. For homogeneous 2D micromodels, Chatzis *et al.*<sup>24</sup> reported pistonlike displacements with very little trapping of the nonwetting phase when the aspect ratio was 2 or less. However, for aspect ratios around 3, large nonwetting phase clusters formed as the wetting phase formed fingers while displacing the nonwetting phase. At higher aspect ratios, the nonwetting phase tended to be trapped in individual pores rather than in large clusters of pores. The pore coordination number had a minor effect on nonwetting phase residual saturations.<sup>24</sup>

Using XMT data, Lindquist *et al.*<sup>23</sup> extensively characterized pore- and throat-size distributions for Fontainebleau sandstones. As core porosity increased from 7.5 to 22%, they found that the average pore coordination number increased from 3.4 to 3.8; the average channel length decreased from 200 to 130  $\mu\text{m}$ ; the average throat area increased from 1,600 to 2,200  $\mu\text{m}^2$ ; and the average pore volume remained fairly constant at approximately 0.0004  $\text{mm}^3$ . The aspect ratio (effective average pore radius/effective average throat radius) was greater than 2 in 65% of pores and greater than 3 in 40%. The aspect ratios tended to increase slightly as porosity decreased.

## Experimental Materials

We performed two sets of imaging experiments with strongly water-wet Berea sandstone cores and one set with a polyethylene core that was strongly oil-wet. (The water-advancing contact angle was measured at 165° for the brine/oil/polyethylene system used in this work.) The Berea cores had permeabilities of  $\sim 0.47$  darcies and porosities of 22%. The polyethylene core had a permeability of 8.8 darcies and a porosity of 40%. (Consistent porosity values were determined from both image analyses and conventional mass-

**TABLE 1—PROPOSED MECHANISMS FOR DISPROPORTIONATE PERMEABILITY REDUCTION**

Proposed Mechanism
1. Gels shrink in oil but swell in water. <sup>4-6</sup>
2. Gravity affects gel locations in pores. <sup>7</sup>
3. Lubrication effects. <sup>8</sup>
4. During brine injection, polymer leaches from the gel and significantly decreases brine mobility. <sup>9</sup>
5. Balance between capillary forces and gel elasticity affects oil and water flow differently. <sup>9,10</sup>
6. Gelants or gels alter rock wettability. <sup>11,12</sup>
7. In a given pore, gels constrict water pathways more than oil pathways. (Wall effects.) <sup>11</sup>
8. Pore blocking by gel droplets. <sup>12,13</sup>
9. Combined wall-effect and gel-droplet model. <sup>13</sup>
10. On a microscopic scale, water and oil follow different pathways. <sup>7,9,12,14</sup>
11. Gels dehydrate when oil is injected. <sup>15</sup>

balance measurements.) The cores were 6.5 mm in diameter and 30 mm in length, with an intermediate pressure tap 6 mm from the inlet face. Our scans focused on a segment of the core that was 6.5 mm in diameter and 3.25 mm in length. To minimize end effects, the scanned segment was located approximately halfway between the inlet and outlet faces. The brine used during the waterfloods contained 1% NaCl and 0.1% CaCl<sub>2</sub>. A hexadecane mixture was used during the oilfloods. To increase the image contrast between the brine and oil phases, hexadecane was doped with 10% w/w iodohexadecane in our first set of experiments in Berea and with 15% w/w bromohexadecane in the second set. For the polyethylene core, the hexadecane was doped with 15% w/w bromohexadecane. All experiments occurred at room temperature. The gelant used in these experiments contained 0.5% Alcoflood 935 HPAM (molecular weight  $\approx 5 \times 10^6$  daltons; degree of hydrolysis = 5 to 10%), 0.0417% Cr(III) acetate, 1% NaCl, and 0.1% CaCl<sub>2</sub>. The gelant viscosity at room temperature was 20 cp. The viscosities were 1.0 cp for brine (without polymer), 3.3 cp for the hexadecane/iodohexadecane mixture, and 3.6 cp for the hexadecane/bromohexadecane mixture.

### Core Characterization

Three-dimensional scans were performed after a gelant flood and after oil and waterfloods both before and after gel placement. (Images were acquired at saturation endpoints.) All floods in a given set of experiments were conducted without removing the core from the sample stand so that the images could be compared directly. For each scan the image was cropped into a 2.97 mm  $\times$  2.97 mm  $\times$  2.1 mm rectangular block (the images were 725  $\times$  725  $\times$  512 voxels at 4.1  $\mu\text{m}/\text{voxel}$ ) to remove artifacts caused by those parts of the core that did not remain within the field of view through all 180° of sample rotation. Image analyses were performed with a software package called 3DMA—a statistical analysis tool that correlates saturations with geometry. This software is capable of measuring distributions of pore size, pore-body/pore-throat aspect ratio, and coordination number from 3D XMT images of porous rock. Specific details on the algorithms used by this software can be found in Ref. 23. Briefly, the software first analyzes an image of a rock containing a single fluid phase in the pore space. A segmentation algorithm that uses the X-ray attenuation coefficient information in the image assigns each cubic volume element (voxel) as either grain or void. A medial axis algorithm is used to trace the percolating backbone (skeleton) of the void space. Properly interpreted, coordination numbers and channel lengths can be obtained directly from the backbone. The backbone is also used as a search device in locating channel throats. (A throat is



**Fig. 1—Image cross section of Berea core saturated with brine. 1.15 mm  $\times$  1.15 mm.**

defined as the smallest cross-sectional area of a channel.) Pore bodies are regions delimited by throats.

Fluid phase location is detected by subtracting X-ray attenuation coefficients in a two-fluid-phase filled image against the corresponding image containing only one of the fluid phases in the void space. (Precision alignment between the two images is required.) As grain/void space identification can be performed on the single fluid-phase image, this (voxel-by-voxel) subtraction is done only for the fluid-filled pore voxels.

To visualize the pore structure and fluid locations, we first focused on thin cross sections with dimensions of 1.15 mm  $\times$  1.15 mm in the *x-y* directions (i.e., perpendicular to the flow direction). **Figs. 1 and 2** illustrate image cross sections for the first Berea core when saturated with brine and for the polyethylene core when

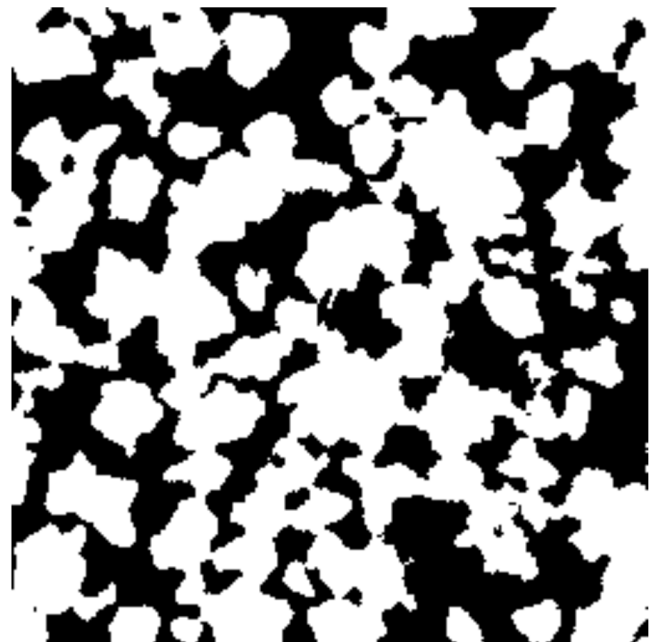


**Fig. 2—Image cross section of polyethylene core saturated with oil. 1.15 mm  $\times$  1.15 mm.**

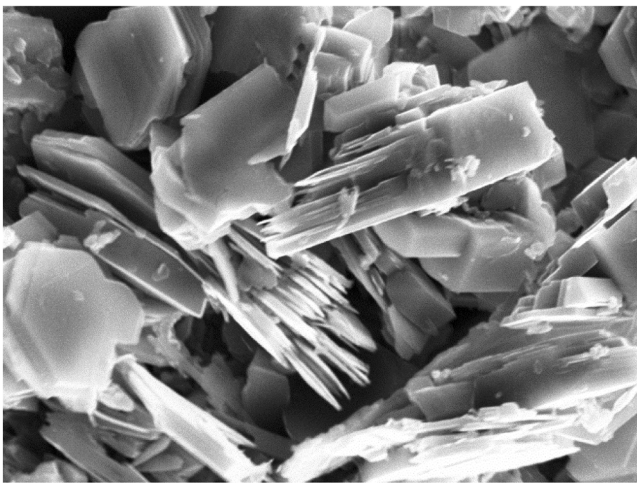


Fig. 3—Scanning electron micrograph of Berea. 30  $\mu\text{m}$  x 22  $\mu\text{m}$ .

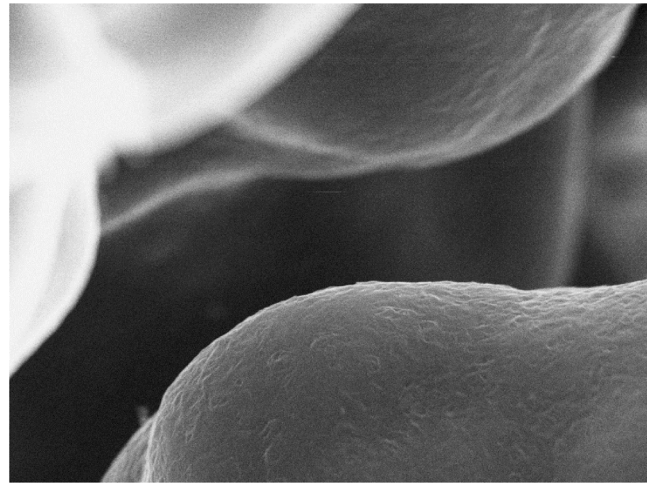


Fig. 4—Scanning electron micrograph of polyethylene. 30  $\mu\text{m}$  x 22  $\mu\text{m}$ .

saturated with oil. The black areas show rock grains or polyethylene. The white areas show brine-saturated voids in the Berea and oil-saturated voids in the polyethylene. These figures highlight the irregular sizes and shapes of the voids. Although the porosity difference is noticeable (22% for Berea and 40% for polyethylene), the pore body and throat sizes were comparable. Electron micrographs (Figs. 3 and 4) were obtained at high magnification for Berea and polyethylene to illustrate the character of the pore walls. (These images were obtained with a Cameca SX100<sup>TM</sup> electron microprobe at New Mexico Tech.) Because of a coating of kaolinite, a significantly greater surface roughness and angularity existed in Berea (Fig. 3) than in the polyethylene core (Fig. 4). Interestingly, before exposure to oil, thin filaments ( $\sim 0.1\text{-}\mu\text{m}$  diameter) bridged many of the small pores in polyethylene. However, these filaments were destroyed upon exposure to hexadecane and were found to be not relevant to our results.<sup>26</sup>

**Size Distributions.** The pore-size distributions for two Berea cores and the polyethylene core are shown in Fig. 5. The y-axis plots the percent of the total number of pores that had a given pore volume (indicated on the x-axis). The distributions (based on pore numbers) were similar for the three cores. For pores with volumes below  $0.0003\text{ mm}^3$ , the fraction of pores of a given size was fairly insensitive to the pore volume. Above  $0.0003\text{ mm}^3$ , the concentration of pores decreased significantly with increased pore volume.

Pore-volume distributions for the three cores are shown in Fig. 6. The y-axis plots the percent of the total void volume that existed

in pores with a given size (indicated on the x-axis). Again, the distributions were quite similar, considering the material differences. The peak in the pore volume occurred at an effective pore radius (assuming spherical pores): approximately  $50\text{ }\mu\text{m}$  for the first Berea core,  $70\text{ }\mu\text{m}$  for the second Berea core, and  $70\text{ }\mu\text{m}$  for the polyethylene core. The average nodal pore volumes for the three cores were very similar to those found by Lindquist *et al.*<sup>23</sup> for Fontainebleau sandstones ( $\sim 0.0004\text{ mm}^3$ ). A comparison of Figs. 5 and 6 reveals that although many pores existed with volumes less than  $0.0001\text{ mm}^3$ , their contribution to the total void volume was small.

**Aspect Ratios.** The distribution of aspect ratios (effective pore radius/effective throat radius) for the Berea and polyethylene cores is shown in Fig. 7. (The effective pore radius computed is for a sphere with a volume equivalent to that measured for the pore. The effective throat radius computed is for a circle with an area equivalent to that measured for the throat.) The y-axis plots the average aspect ratio in pores with a given size (indicated on the x-axis). Again, the distributions were surprisingly similar for the cores. The average aspect ratio was 4.0 for the first Berea core, 4.2 for the second Berea core, and 4.4 for the polyethylene core. As pore volume increased from  $10^{-5}\text{ mm}^3$  (effective pore radius  $\sim 13\text{ }\mu\text{m}$ ) to  $0.002\text{ mm}^3$  (effective pore radius  $\sim 78\text{ }\mu\text{m}$ ), the average aspect ratio increased steadily from 2 to 6. Aspect ratios jumped sharply for the few largest pores. For a given pore size, a wide range of aspect ratios were noted. For all cores at a given pore size, the

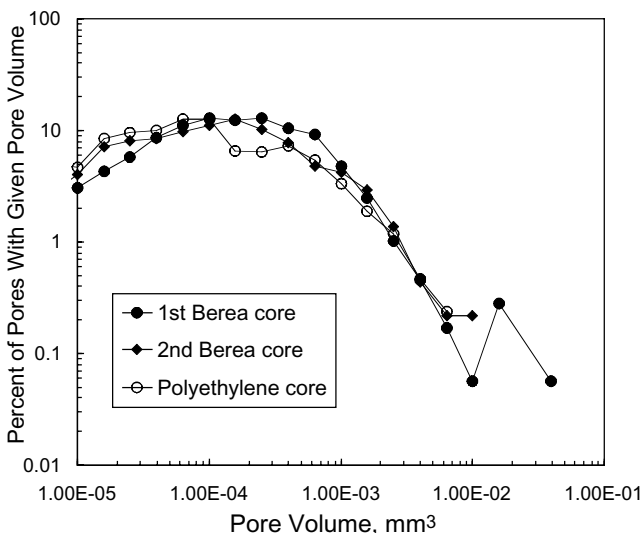


Fig. 5—Pore-size distributions.

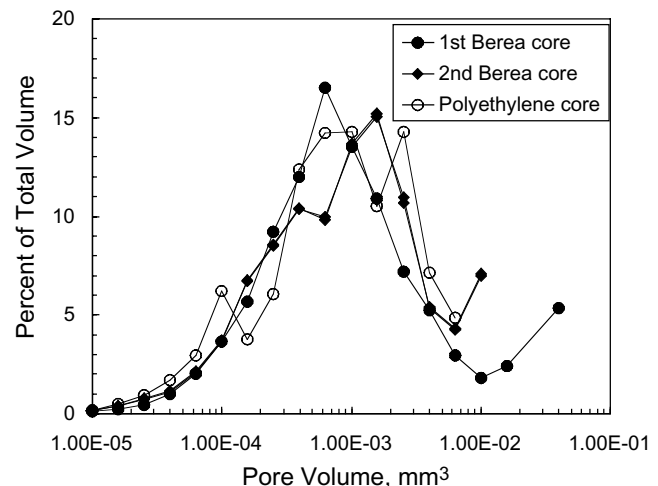


Fig. 6—Pore-volume distributions.

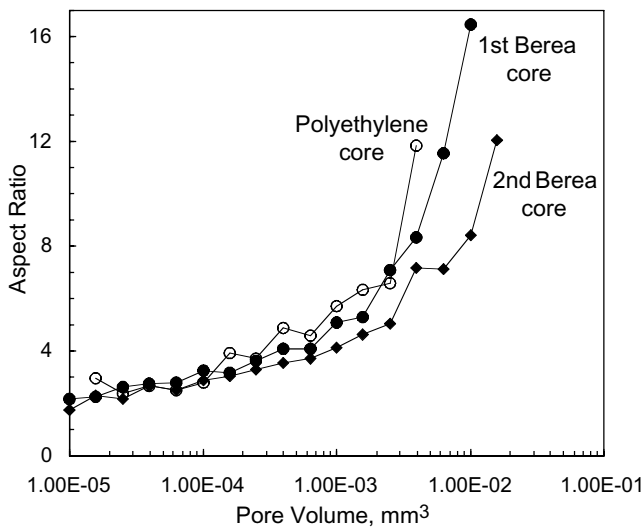


Fig. 7—Aspect-ratio distributions.

standard deviation (of aspect ratios) was typically 65% of the mean value.

For Berea sandstone, Fig. 8 plots the distributions of aspect ratios for each of four ranges of pore volume (PV): (1)  $PV > 0.01 \text{ mm}^3$ ; (2)  $0.001 < PV < 0.01 \text{ mm}^3$ ; (3)  $0.0001 < PV < 0.001 \text{ mm}^3$ ; and (4)  $PV < 0.0001 \text{ mm}^3$ . The x-axis plots various ranges of aspect ratio,  $R$ , from  $R < 2$  up to  $R > 30$ . The y-axis plots the percent of the total aspect ratios (for a given PV range) that fall within a given range of aspect ratios. The solid and open triangles in Fig. 8 show that approximately 35% of the smallest pores were associated with aspect ratios that were less than 2. Interestingly, for all four pore-size ranges, 25 to 35% of the aspect ratios fell between 3 and 5, and a significant percentage of aspect ratios fell between 5 and 10. Aspect ratios above 10 were common for the larger pores but were rare for the smaller pores. In contrast, aspect ratios below 3 were very common for the smaller pores but were much less frequent for the larger pores.

The average throat area was  $1,330 \mu\text{m}^2$  for the first Berea core,  $1,460 \mu\text{m}^2$  for the second Berea core, and  $1,630 \mu\text{m}^2$  for the polyethylene core. These values were generally lower than the average throat areas reported for Fontainebleau sandstones ( $1,600$  to  $2,200 \mu\text{m}^2$ ).<sup>23</sup>

**Coordination Numbers.** The distributions of pore coordination numbers are shown in Fig. 9. (The coordination number is the

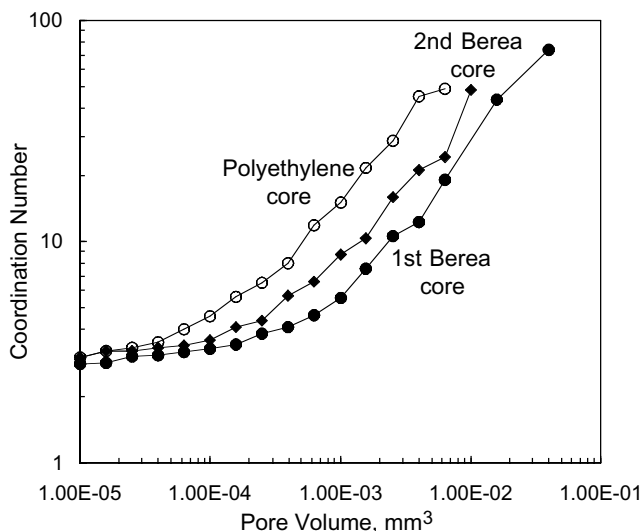


Fig. 9—Coordination number distributions.

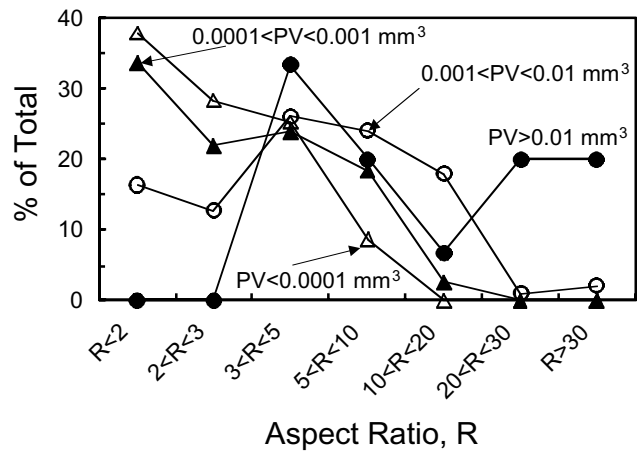


Fig. 8—Aspect ratios in Berea.

number of exits from a pore.) The y-axis plots the average coordination number in pores with a given size (indicated on the x-axis). The average coordination number was 3.9 for the first Berea core, 4.7 for the second Berea core, and 6.2 for the polyethylene core. For the smallest pores, the coordination number was approximately 3 for all three cores. As the pore size increased, the coordination numbers increased, with the polyethylene core experienc-

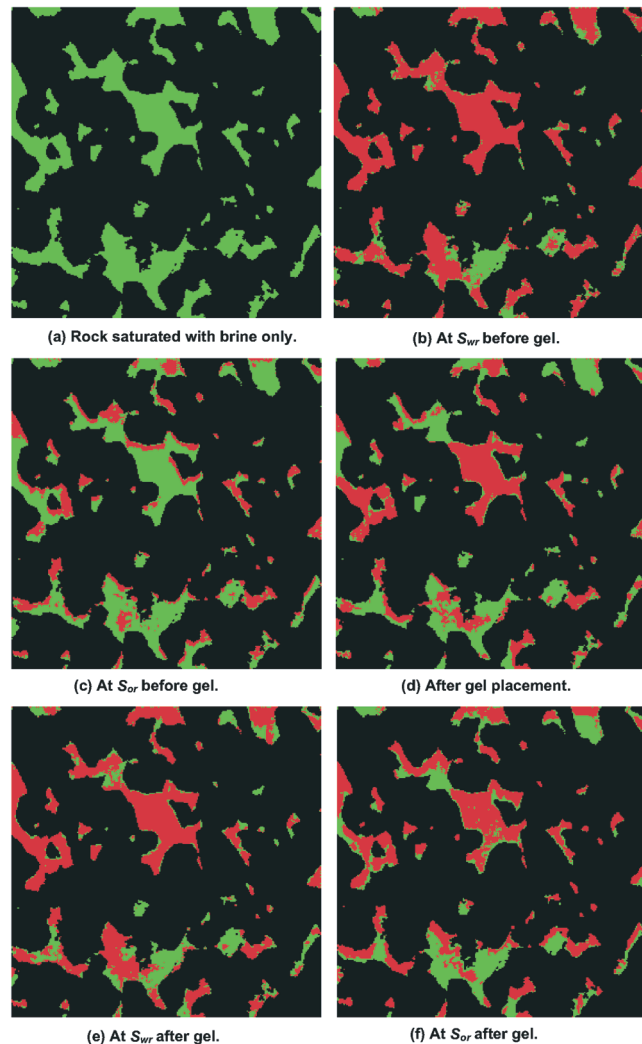


Fig. 10—Berea sandstone cross-sectional image slices ( $1.15 \text{ mm} \times 1.15 \text{ mm}$  each). Green is water. Red is oil. Black is rock.

ing a slightly more rapid increase than the Berea cores. Coordination numbers up to 70 were noted for the largest pores. For a given pore size, standard deviations were typically 20 to 40% of the mean values.

Ioannidis *et al.*<sup>27</sup> reported comparable properties for Berea sandstone based on analyses of photomicrographs of 78 serial sections through a double pore cast of a Berea sample. Their analyses of 1,268 pores and 1,945 throats indicated that the average coordination number was 3.46—somewhat lower than our values. Their average throat area was 60 to 90% greater than our values, and their pore-size distribution was weighted toward larger pores than our distributions.

### Images After the Various Floods

XMT scans were performed after each flood. Fig. 1 and Fig. 10 show image slices for the first Berea core for each of the flooding stages. Figs. 2 and 11 show image slices for the various flooding stages in the polyethylene core. In Figs. 10 and 11, oil is red, water is green, and the rock grains (or polyethylene) are black. To magnify the pore structure, these cross sections are 1.15 mm × 1.15 mm. Corresponding fluid saturations and permeabilities associated with the floods are listed in Tables 2 and 3. For several cases in Figs. 10 and 11, small isolated oil drops or thin oil filaments (in red) appear floating in water (in green) within a single pore. In other cases, isolated water drops or thin water filaments appear floating in oil within a single pore. We recognize that multiple droplets and suspended liquid filaments are unlikely in individual pores. The chief origin of these artifacts is our current segmenta-

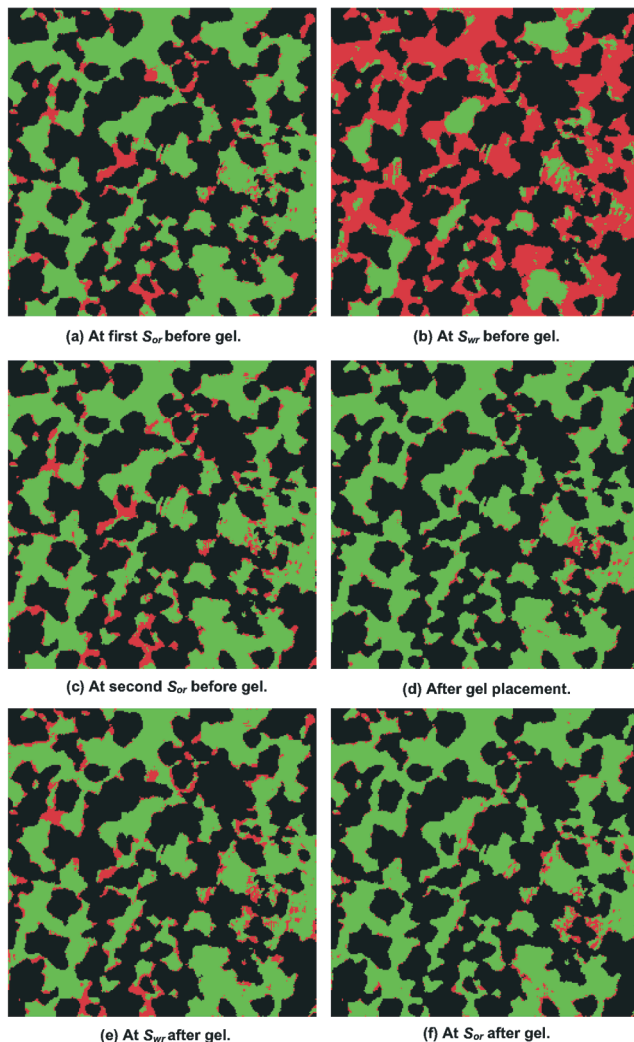


Fig. 11—Polyethylene cross-sectional image slices (1.15 mm × 1.15 mm each). Green is water. Red is oil. Black is polyethylene.

TABLE 2—FLUID SATURATIONS

	1st Berea Core	2nd Berea Core	Polyethylene Core
Permeability, darcies	0.47	0.48	8.8
Porosity, %	22	22	40
First saturated with:	water	water	oil
$S_w$ at 1st $S_{wr}$ , %	24.7	37.3	0.0
$S_w$ at 1st $S_{or}$ , %	56.5	56.8	77.7
$S_w$ at 2nd $S_{wr}$ , %		34.3	15.2
$S_w$ at 2nd $S_{or}$ , %			75.0
$S_w$ at 1st $S_{or}$ after gel, %	47.7		94.4
$S_w$ at $S_{wr}$ after gel, %	29.0		75.7
$S_w$ at 2nd $S_{or}$ after gel, %	21.3		92.4

tion method, which was used to distinguish between oil and water phases. Recall that fluid-phase identification is made by subtracting two corresponding images: one with a single phase in the void space, the other having both fluid phases present (one phase of which is doped with a strong X-ray attenuating compound). A histogram of the subtracted X-ray attenuation coefficients will show a bimodal distribution, with the peaks corresponding, respectively, to water- and oil-filled voxels. The peaks in this histogram will overlap. There are several reasons for the overlap: the finite size of a voxel means that any X-ray attenuation coefficient measured is an average over the voxel volume; variation in X-ray counting statistics results in variations in attenuation coefficients; and minor alignment errors, on the order of 1/2–1 voxel width, do occur.

Currently, we use simple thresholding to distinguish between water- and oil-filled voxels. The threshold is determined from an examination of the bimodal subtraction histogram, with the threshold value picked to lie in the “valley” between the two peaks. Simple thresholding is well known to result in speculated images (i.e., apparent blobs of one phase trapped in the other). The extent of the speculation is proportional to the overlap between the two peaks in the difference histogram. Examination of our data indicates that such speculation accounts for less than 6% of the volume of any one phase. Note additionally that caution must be observed in evaluating the amount of speculation by viewing only 2D slices such as Figs. 10 and 11. Often, what appears as a disconnected blob in two dimensions is a piece of a shaped surface of a much larger 3D structure. In fact, this can be noticed in Fig. 1, which appears to show a few disconnected grain segments. Analysis of the full 3D image indicates no disconnected grains.

### Berea Sandstone Image Analyses

**Before Gelant Injection.** In the first Berea core, the first scan viewed the core with 100% brine saturation (Fig. 10a). Second, the

TABLE 3—PERMEABILITIES

	1st Berea Core	2nd Berea Core	Polyethylene Core
Permeability, darcies	0.47	0.48	8.8
Porosity, %	22	22	40
First saturated with:	water	water	oil
$k_{ro}$ at 1st $S_{wr}$	0.82	0.79	1.0
$k_{rw}$ at 1st $S_{or}$	0.16	0.18	0.50
$k_{ro}$ at 2nd $S_{wr}$		0.78	0.45
$k_{rw}$ at 2nd $S_{or}$			0.49
$F_{rro}$	15		24
$F_{rrw}$	1,220		2,130
$F_{rrw}/F_{rro}$	81		89

core was flooded with ~35 core pore volumes of oil and scanned at residual water saturation (Fig. 10b). Oil invaded most pores, while the residual water appeared dominantly in crevices and films between the oil and the rock. The residual water saturation,  $S_{wr}$ , was 24.7% (Table 2), and the endpoint relative permeability to oil (relative to the absolute permeability),  $k_{ro}$ , was 0.82 (Table 3). Third, the core was flooded with water (~70 core pore volumes) and scanned at residual oil saturation (Fig. 10c). Pores appear with a range of saturations (i.e., individual pores are not necessarily nearly all oil-filled or nearly all water-filled). The residual oil saturation,  $S_{or}$ , was 43.5% (i.e., 100%–56.5%, from Table 2), and the endpoint relative permeability to water,  $k_{rw}$ , was 0.16. These findings are consistent with expectations in a strongly water-wet rock.

Using the 3DMA software, detailed analyses were performed with the complete 3D images (not just the 2D slices shown in Figs. 10 and 11). The distributions of water and oil saturations were determined as a function of pore size. In Fig. 12, the solid symbols show the distribution of water saturations ( $S_w$ ) at  $S_{wr}$  before gel placement. (In this figure and subsequent figures, average saturations for a given pore size are reported.) The open symbols show the distribution of water saturations at  $S_{or}$  before gel placement. (Of course, at any condition, the oil saturation is equal to 100% minus the water saturation.) As mentioned, the overall average  $S_{wr}$  was 24.7% for the first Berea core. This number was consistent with the  $S_{wr}$  values measured using mass balances in this strongly water-wet Berea sandstone. As expected at  $S_{wr}$ , the water saturation generally increased with decreased pore size (solid circles in Fig. 12). A broad minimum in water saturation was noted around 0.002 mm<sup>3</sup>, and a local maximum was observed around 0.01 mm<sup>3</sup>. For a strongly water-wet porous medium, one might have expected the water saturation to approach 100% for the smallest pores. Instead, the water saturation in the smallest pores averaged 60%. A calculation using the Young-Laplace equation confirmed that oil should be able to enter the small pores (i.e., PV ~10<sup>-5</sup> mm<sup>3</sup>) in our Berea cores. Specifically, to enter the smallest pore throats (~7 μm), a capillary pressure around 1 psi was needed. This value was much lower than the 17 psi (pressure drop across the core) that was applied during our flooding experiments. The behavior of  $S_w$  vs. pore size was confirmed during an imaging experiment in a second Berea core (solid squares in Fig. 12). This experiment included a second oilflood (following an intervening waterflood). Results from this part of the experiment (solid triangles in Fig. 12) further confirmed the above behavior and indicated limited hysteresis during cycles of water- and oilflooding before gel placement. The fluid saturations and relative permeabilities from this second Berea core (Tables 2 and 3) also suggest that little hysteresis occurred during multiple flooding cycles.

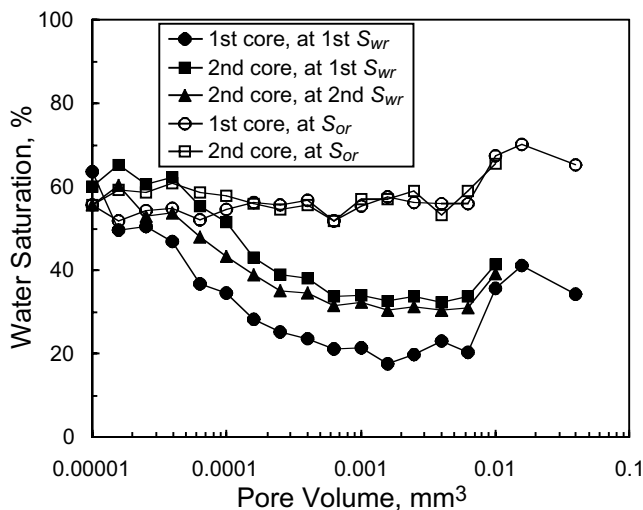


Fig. 12—Water saturations at  $S_{wr}$  and  $S_{or}$  before gel placement in Berea sandstone cores.

As mentioned, the overall average  $S_{or}$  was 43.5% for the first Berea core. This number was significantly higher than the  $S_{or}$  values measured with mass balances in this strongly water-wet Berea sandstone (~22%). At  $S_{or}$ , the average water saturation was surprisingly insensitive to pore size (open circles in Fig. 12). These results were confirmed during imaging studies of our second core (open squares in Fig. 12).

For a given pore size, Fig. 12 shows the average water saturation from a given experiment. Of course, because many pores were present for any given pore size, a range of saturations was found. A detailed examination of the data revealed that for a given pore size, the range or distribution of water saturations was quite broad, both at  $S_{or}$  and at  $S_{wr}$ . One feature of these XMT studies is that we can monitor the saturation differences for individual pores from one flooding stage to the next. Because of space limitations, this level of detail is not reported here but can be found in Ref. 26. For example, at  $S_{or}$ , virtually all pores contained at least 20% oil, and half the pores contained at least 45% oil. Chatzis *et al.*<sup>24</sup> noted that for pore-body/pore-throat radius aspect ratios around 3, the non-wetting phase tends to be trapped in large clusters of pores. In contrast, for ratios exceeding 3, the nonwetting phase tends to be trapped in individual pores. We noted that 75% of our pores had aspect ratios exceeding 2, and 56% had ratios exceeding 3.

While oil saturations at values intermediate between 0 and 1 would be unexpected in a medium containing only spherical pores, the images in Figs. 1 through 4 and Figs. 10 and 11 show that the pore shapes are typically elongated and asymmetric, containing corners, nooks, and crannies. The combination of individual pore trapping and irregular pore-body shapes allows for a wide range of intermediate saturations for individual pores.

Because our cores were small (30 mm in length), the capillary end effect could have created a saturation gradient through the core. Three factors worked in our favor to minimize this effect. First, the image volume was located near the center of the core, maximizing distance from the inlet and outlet faces. Second, our cores were quite permeable (0.47 darcies for Berea and 8.8 darcies for polyethylene). Third, our floods were conducted with relatively high capillary numbers and pressure gradients (17 to 35 psi/ft). Examination of our images (which cover approximately 7% of the core length) revealed no obvious saturation trend in any direction. Nevertheless, we cannot discount the possibility that a saturation gradient might have existed in the cores.

One also might wonder whether our small image volume (~19 mm<sup>3</sup>) was less than the representative elementary volume (REV) for this porous medium. We are unable to answer this question definitively. Our Berea images contained 1,700 to 1,800 pores that were larger than 10<sup>-5</sup> mm<sup>3</sup>. Those who advocate the REV concept might argue that at least 1 million pores (i.e., 100 grain diameters per side of the sample volume) are needed to form an REV. Obviously, our image volume does not meet this criterion. On the other hand, the observations that we report in this paper appear to be generally valid throughout the imaged volumes (i.e., we did not observe regions of exceptional behavior within a given image volume). This point can be appreciated in part by considering Figs. 10 and 11.

**During Gelant Injection.** After establishing a residual oil saturation in the first Berea core, the 20-cp Cr(III)-acetate-HPAM gelant (10 core pore volumes) was injected with a pressure gradient of 17 psi/ft. After gel placement, the core was shut in for 12 hours (at 60°C) and then scanned (at room temperature). The gelation time for this formulation was 1 to 1.5 hours at 60°C.

A comparison of Figs. 10c and 10d suggests that fluid saturations changed somewhat during gelant injection. A detailed analysis of the 3D images (Fig. 13) confirmed that fluid saturations changed during gelant injection. The open and solid circles in Fig. 13 reveal that average water saturations decreased slightly in the medium-to-large pores during gelant injection in Berea. Also, the overall average water saturation decreased from 56.5 to 47.7% (Table 2). On first consideration, these observations surprisingly suggest that oil was generated when gelant (containing no oil) was injected. However, the reader should recall that the imaged volume

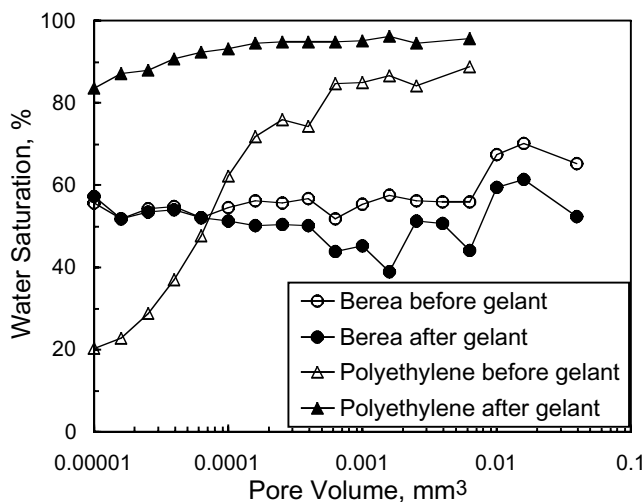


**Fig. 13—Water saturations at  $S_{or}$  immediately before vs. immediately after gel placement.**

constituted only 10% of the total core volume. Conceivably, oil was displaced from upstream portions of the core during gelant injection, and this oil became trapped in the imaged volume by coincidence. Presumably, the overall oil content of the core either stayed the same or decreased slightly during gelant injection.

**After Gel Placement.** After gel placement, oil (~20 core pore volumes) was injected to measure the oil residual resistance factor,  $F_{rro}$ , recording a value of 15. This value means that at  $S_{wr}$ , the gel reduced the permeability to oil by a factor of 15. The core was scanned after oil injection to visualize oil pathways after gel (Fig. 10e). A comparison of Figs. 10b and 10e indicates that most of the pathways open to oil flow before gel placement remained accessible to oil after the gel treatment. This result suggests that after oil injection, the gel occupied only a small fraction of the pore space. Tracer results from a previous experiment in a high-permeability Berea core revealed that gel with an  $F_{rro}$  value of 20 occupied less than 5% of the pore space.<sup>1</sup>

The solid symbols in **Fig. 14** compare distributions of water saturations at  $S_{wr}$  before and after gel placement. The two distributions were remarkably similar, confirming that most of the pathways that were open to oil flow before gel placement were also open to oil flow after gel placement. As mentioned earlier, this suggestion is consistent with the relatively low oil residual resistance factor (i.e., 15). Because the gel was placed and formed at high water saturation in the core, the result also suggests either (1) that gel did not form in all the aqueous pore space (i.e., gelation

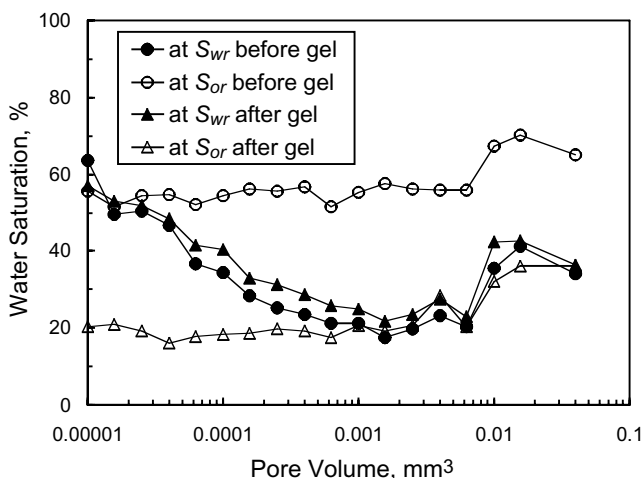


**Fig. 14—Effect of gel on  $S_{wr}$  and  $S_{or}$  in Berea sandstone.**

was incomplete) or (2) that oilflooding after gel placement moved, concentrated, or destroyed much of the gel that formed in the oil pathways.

Finally, brine (2.5 core pore volumes) was injected to measure the water residual resistance factor,  $F_{rrw}$ . The  $F_{rrw}$  value was 1,220, meaning that at  $S_{or}$ , the gel reduced the permeability to water by a factor of 1,220. This gel reduced the permeability to water 81 times more than that to oil ( $F_{rrw}/F_{rro}=81$ ). Fig. 10f shows the core scan after brine injection. A comparison of Figs. 10c and 10f shows that water did not have access to most of the pathways that were open to oil flow after the gel treatment.

The open symbols in Fig. 14 compare distributions of water saturations at  $S_{or}$  before and after gel placement. For reasons yet to be explained, water saturations in the smallest pores (<0.0005 mm<sup>3</sup>) at  $S_{or}$  after gel placement were less than those at  $S_{wr}$ . However, more importantly (because the total pore volume was dominated by the largest pores), the distribution of water saturations in the largest pores (>0.001 mm<sup>3</sup>) after gel placement during waterflooding (open triangles) was similar to that during the previous oilfloods (solid symbols in Figs. 12 and 14). Therefore, the gel treatment apparently trapped substantial additional volumes of oil during waterflooding (i.e., much higher  $S_{or}$  values). Perhaps this result occurred because gel was strategically positioned in pore throats to increase aspect ratios. With most pores permanently occupied by oil, water was forced to flow through thin films, through the smallest pores, and through the gel itself, explaining the large water residual resistance factor (i.e., 1,220). In contrast, oil pathways remained relatively free from constriction by the gel, so the oil residual resistance factor was much less (i.e., 15).

### Polyethylene Image Analyses

**Before Gelant Injection.** In the polyethylene core, the first scan viewed the core with 100% oil saturation (Fig. 2). Second, the core was waterflooded (~70 core pore volumes) and scanned at residual oil saturation (Fig. 11a). Water invaded most pores, while the residual oil appeared dominantly in small pores and films between water and the polyethylene. The oil films were less evident than the water films in Berea (compare Figs. 10b and 11a); however, careful examination reveals that the oil films were present on the polyethylene. In reality, the liquid films should be much thinner than we can resolve with the XMT method. The appearance that water films on Berea sandstone were thicker than oil films on polyethylene may be caused by the greater surface roughness in Berea (compare Figs. 3 and 4). Greater surface roughness creates folds of the film and fluid accumulations in nooks and crannies. Although the actual film thickness may be only a few tens of nanometers at a given point, the film folds and small fluid accumulations are interpreted to be much wider with our imaging technique because the resolution is limited to the micrometer scale.

Third, oil (~35 core pore volumes) was injected to drive the core to residual water saturation (Fig. 11b). Residual water was noted in pores with a wide range of sizes. Also, water often appeared at the polyethylene interface, suggesting either very thin oil films or partial water wetting of the plastic.

Water (~70 core pore volumes) was again injected to establish  $S_{or}$  (Fig. 11c). The similarity of Figs. 11a and 11c indicates little hysteresis during the cycle of water and oil injection. The similarity of water saturations (77.7% vs. 75.0%) and relative permeabilities (0.50 vs. 0.49) for the two waterfloods at  $S_{or}$  supports this suggestion (Tables 2 and 3). **Fig. 15** provides additional support. This figure plots water saturations as a function of pore size before gelant injection. The solid circles show the distribution of water saturations at  $S_{wr}$  before gel placement. The open circles and triangles show the two distributions at  $S_{or}$ . The similarity of the two distributions at  $S_{or}$  confirms that hysteresis was not significant.

A comparison of Figs. 12 and 15 reveals significant differences in the saturation distributions for Berea vs. polyethylene. Most notably, the intermediate-to-large pores exhibited a substantially greater saturation difference between  $S_{wr}$  and  $S_{or}$  for polyethylene (~15% vs. ~85%) than for Berea (~30% vs. ~60%). For the smallest pores in both porous media, the distributions at  $S_{wr}$  converged with those at  $S_{or}$ . However, the water saturation for this conver-

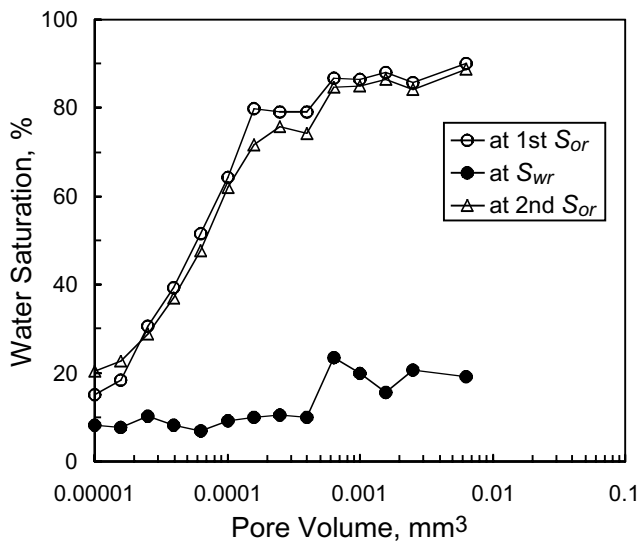


Fig. 15—Water saturations at  $S_{wr}$  and  $S_{or}$  before gel placement in the polyethylene core.

gence occurred at a significantly lower value for polyethylene (10 to 20%) than for Berea (50 to 60%). For polyethylene, the average water saturation at  $S_{wr}$  was nearly independent of pore size. In contrast, in Berea, the average water saturation at  $S_{or}$  was nearly independent of pore size. For polyethylene at  $S_{or}$ , the water saturation increased significantly with increased pore size. In contrast, for Berea at  $S_{wr}$ , the water saturation decreased significantly with increased pore size. Presumably, these differences reflect the preference for water to occupy the smallest pores in water-wet Berea and not to occupy the smallest pores in the oil-wet polyethylene (i.e., because the ratio of surface area to volume increased with decreased pore size).

**During Gelant Injection.** In the next step, gelant (10 core pore volumes) was injected with a pressure gradient of 23 psi/ft. After gel placement, the core was shut in for 14 hours (at  $\sim 70^\circ\text{C}$ ) and scanned (at room temperature). A comparison of Figs. 11c and 11d indicates that oil was mobilized during gelant injection. Immediately after gel placement, most remaining oil appeared as a film attached to the polyethylene. Although a water residual resistance factor was not measured at this point, in a separate study,<sup>13</sup> an  $F_{rrw}$  value of 25,000 was measured for this gelant and core material immediately after gel placement. This high residual resistance factor indicated that the gel occupied virtually all of the aqueous pore space and reduced the core permeability to approximately 0.2 md.

A detailed analysis of the 3D images (Fig. 13) confirmed that fluid saturations changed during gelant injection. The open and solid triangles in Fig. 13 reveal that average water saturations increased substantially in the small-to-medium pores during gelant injection in polyethylene. Also, the overall average water saturation increased from 75.0 to 94.4% (Table 2). On the one hand, an increase in water saturation might be expected because the injected gelant was 20 times more viscous than the displaced water. However, on the other hand, the pressure gradient during gelant placement (23 psi/ft) was intentionally kept below that used during the other flooding steps (35 psi/ft) to avoid mobilization of the residual phase. Three arguments could be offered to rationalize the observed behavior. First, because polyethylene was oil-wet, a continuous oil film may have existed throughout the porous medium. Thus, true irreducible oil saturation may not exist. With increased gelant or water throughput, oil in the continuous film may be able to drain slowly from the porous medium. A second explanation is that the gelant may have changed the wettability of the porous medium to more water-wet. However, although some argue in favor of this type of mechanism,<sup>28</sup> it is counterintuitive and requires much more convincing support. A third possible mechanism was suggested by Wang *et al.*<sup>29</sup> Specifically, at a fixed capillary

number, viscoelastic polymer solutions (e.g., our gelant) redistribute forces on a microscopic scale in a manner that drives residual phases to lower-than-expected values. These possibilities will be explored during future work.

**After Gel Placement.** After the shut-in period, oil (20 core pore volumes) was injected, and a value of 24 was measured for the oil residual resistance factor. This value was quite similar to the corresponding value measured in Berea (15, from Table 3). However, a comparison of the XMT scans (Figs. 10e and 11e) suggests that the oil saturations and oil pathways were very different in polyethylene from those in Berea. In Berea, the overall oil saturation was quite high (71%, from Table 2). In polyethylene, the oil saturation was much lower (24.3%, from Table 2). Interestingly, the oil locations in Fig. 11e were very similar to those in Figs. 11a and 11c. Thus, in polyethylene, the oil locations during oil injection after gel placement were virtually the same as those during water injection before gel placement. This observation receives further support from the plots of water saturation vs. pore size. In Fig. 16, the saturation distribution at  $S_{or}$  before gel placement (open circles) was virtually the same as that at  $S_{wr}$  after gel placement (solid triangles).

Finally, water (2.5 core pore volumes) was injected, and a value of 2,130 was measured for  $F_{rrw}$ . This value was comparable to that for Berea (1,220, from Table 3). Also, the ratio  $F_{rrw}/F_{rro}$  was 89 in polyethylene vs. 81 in Berea. Despite the similarity of  $F_{rrw}$  values, the water saturations and water pathways appear very different in polyethylene from those in Berea (compare Figs. 10f and 11f). In Berea, a comparison of Figs. 10e and 10f suggests that the dramatic permeability reduction for water was caused by gel trapping a high residual oil saturation. In contrast, in polyethylene (Fig. 11f), the oil saturation was very low (7.6%, from Table 2). Interestingly, the images shown in Figs. 11d and 11f are very similar. This observation receives further support from the plots of water saturation vs. pore size. The saturation distribution at  $S_{or}$  immediately after gel placement (solid triangles in Fig. 13) was very similar to that after the final waterflood after gel placement (open triangles in Fig. 16).

Presumably during gelant injection, virtually all water was displaced by the aqueous gelant. As mentioned earlier, some residual oil also was displaced. After gelation, an effective gel permanently occupied locations that were previously occupied by water at  $S_{or}$  before gelant injection. Thus, oil could no longer flow through those locations. The only flow paths available for oil were those through locations that were occupied by oil at  $S_{or}$  before gelant injection. This scenario explains why the distribution of saturations at  $S_{or}$  before gelant injection was the same as that at  $S_{wr}$  after gel

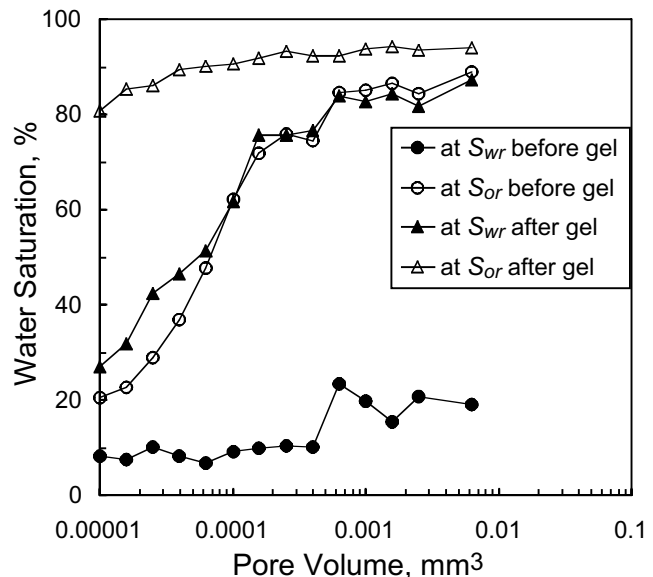


Fig. 16—Effect of gel on  $S_{wr}$  and  $S_{or}$  in polyethylene.

placement (Figs. 11c, 11e, and 16). However, at the condition associated with  $S_{or}$ , why should oil be able to flow at all? Perhaps a continuous oil film on the polyethylene allowed flow (i.e., the oil was not trapped as discontinuous drops at  $S_{or}$ ). Considering that  $F_{rro}$  was 24 for this experiment, the above suggestion implies that if no gel was present, the permeability to oil at a water saturation of 75.7% (from Table 2) should be 24 times less than the permeability to oil at a water saturation of 15.2%. In other words, perhaps our core was not at true irreducible oil saturation when water was injected. We will explore this possibility in future work.

Recall that the process of gel placement drove  $S_{or}$  from 25.0 to 5.6% (Table 2). However, during oilflooding after gel placement, oil returned to those locations where gelant had previously removed residual oil (see Figs. 11c through 11e and Figs. 13 and 16). Why did gel not block these locations permanently? Considering the size of these locations (red areas of Figs. 11c through 11e) and the inert nature of polyethylene, it seems likely that gel formed here as effectively as in other locations. Possibly, during the oil-flood after gel placement, the topography of the porous medium, combined with capillary forces, allowed the oil to rip<sup>9,10</sup> or dehydrate<sup>15</sup> gel to form pathways in the regions occupied by the original oil saturation. As mentioned earlier, this mechanism also may have been operable in Berea. However, in Berea, the gel trapped oil associated with saturations at  $S_{wr}$  before gel placement. In polyethylene, the gel trapped oil associated with saturations at  $S_{or}$  before gel placement.

After gel placement, the permeability to water was dramatically less than that to oil. This result suggests that the largest oil pathways shown in Figs. 11c and 11e generally were not open to water flow. Why not? One proposed possibility was that a new residual oil saturation was established in these pathways during the final waterflood.<sup>15</sup> However, careful examination of Figs. 11c through 11f and Figs. 13 and 16 reveals that this did not happen. A second possibility is that elastic forces associated with the gel closed the largest oil pathways during the final waterflood.<sup>9,10</sup> In this theory, capillary forces keep the oil pathways open during oilflooding.<sup>9,10</sup> A third possibility is that the oil pathways were open during oilflooding but closed during waterflooding because gels “shrink in the presence of oil but swell in the presence of water.”<sup>4-6</sup> This proposed mechanism is troubling because in the absence of osmotic effects, the available evidence indicates that our gels do not shrink in the presence of oil and swell in the presence of water.<sup>7,9</sup>

Of course, additional work will be performed to address the questions and test the hypotheses raised in this paper.

## Relevance to Field Applications

When production wells were treated with gelants, some zones had high water saturations and high fractional water flows, while other zones had high hydrocarbon saturations and fractional flows. For the oil zones, the flooding sequence used for this paper mimics the field situation. Specifically, oil was the first fluid to flow through the gel after the treatment. Thus, the oil residual resistance factor of 15 and the mechanism for establishment of oil permeability through the gel are relevant to field applications.<sup>1-3</sup> However, this is not the case for the water zones. Specifically, in water zones in field treatments, water was the first fluid to flow through the gel after gel placement (i.e., no oil flowed through the gel in the water zones). For this circumstance, our previous experience with Cr(III)-acetate-HPAM gels revealed that water residual resistance factors were ~10,000 and that the gel occupied virtually all of the aqueous pore space.<sup>1,2</sup> Thus, the mechanism for water permeability reduction in field applications is actually one of near-total blockage of water flow. Virtually the only means for water flow is through the gel itself (which has a permeability less than 1 md).<sup>16,27</sup> In contrast, in the experiments here, the mechanism of water flow was examined after oil flowed through the gel. Nevertheless, because the water residual resistance factor in these experiments was 80 to 90 times greater than the oil residual resistance factor, the mechanism of permeability reduction for water is of scientific interest.

## Conclusions

X-ray computed microtomography was used to investigate why gels reduce permeability to water more than that to oil in strongly water-wet Berea sandstone and in an oil-wet porous polyethylene core. The following conclusions were reached:

1. Although the two porous media had very different porosities (22% vs. 40%), the distributions of pore sizes and aspect ratios were similar.
2. A Cr(III)-acetate-HPAM gel caused comparable oil and water permeability reductions in both porous media. In both cores, the gel reduced permeability to water by a factor 80 to 90 times more than that to oil.
3. The distributions of water and oil saturations (vs. pore size) were substantially different before, during, and after gel placement.
4. The disproportionate permeability reduction appeared to occur by different mechanisms in the two porous media. In Berea, gel caused disproportionate permeability reduction by trapping substantial volumes of oil that remained immobile during waterflooding. With this high trapped-oil saturation, water was forced to flow through thin films, through the smallest pores, and through the gel itself. In contrast, during oilflooding, oil pathways remained relatively free from constriction by the gel.
5. In the polyethylene core, oil trapping did not contribute significantly to the disproportionate permeability reduction. Instead, oil films and a relatively small number of pore pathways provided conduits for the oil. For reasons yet to be understood, the small pore pathways appeared largely unavailable for water flow.

## Nomenclature

$F_{rr}$	= residual resistance factor
$F_{rro}$	= residual resistance factor for oil
$F_{rrw}$	= residual resistance factor for water
$k_{ro}$	= relative permeability to oil
$k_{rw}$	= relative permeability to water
$R$	= aspect ratio
$S_{or}$	= residual oil saturation, %
$S_w$	= water saturation, %
$S_{wr}$	= residual water saturation, %

## Acknowledgments

Financial support for this work is gratefully acknowledged from the Natl. Petroleum Technology Office (NETL) of the U.S. Dept. of Energy, BP, Chevron, China Natl. Petroleum Corp., Chinese Petroleum Corp., Marathon, Shell, and Texaco. The efforts of John Hagstrom were appreciated during the corefloods and imaging experiments. We also thank Jill S. Buckley (New Mexico Tech) for helpful discussions and suggestions and Nelia Dunbar (New Mexico Tech) for obtaining the electron micrographs. This research was carried out (in part) at the Natl. Synchrotron Light Source, Brookhaven Natl. Laboratory, which is supported by the U.S. Dept. of Energy, Division of Materials Sciences and Division of Chemical Sciences. The Geosciences Program of the U.S. Dept. of Energy (grant DE-FG02-92ER14261) funded development of the 3DMA code.

## References

1. Liang, J., Sun, H., and Seright, R.S.: “Reduction of Oil and Water Permeabilities Using Gels,” paper SPE 24195 presented at the 1992 SPE/DOE Symposium on Enhanced Oil Recovery, Tulsa, 22–24 April.
2. Seright, R.S., Liang, J., and Sun, H.: “Gel Treatments in Production Wells with Water Coning Problems,” *In Situ* (1993) **17**, No. 3, 243.
3. Liang, J., Lee, R.L., and Seright, R.S.: “Gel Placement in Production Wells,” *SPEPF* (November 1993) 276; *Trans.*, AIME, **295**.
4. Sparlin, D.D. and Hagen, R.W. Jr.: “Controlling Water in Producing Operation—Part 5,” *World Oil* (July 1984) 137.
5. Dawe, R.A. and Zhang, Y.: “Mechanistic Study of the Selective Action of Oil and Water Penetrating into a Gel Emplaced in a Porous Medium,” *J. Pet. Sci. Eng.* (1994) **12**, 113.

6. Mennella, A. *et al.*: "Pore-Scale Mechanism for Selective Permeability Reduction by Polymer Injection," paper SPE 39634 presented at the 1998 SPE/DOE Improved Oil Recovery Symposium, Tulsa, 19–22 April.
7. Liang, J., Sun, H., and Seright, R.S.: "Why Do Gels Reduce Water Permeability More Than Oil Permeability?" *SPE* (November 1995) 282; *Trans.*, AIME, **299**.
8. Zaitoun, A., Rahbari, R., and Kohler N.: "Thin Polyacrylamide Gels for Water Control in High-Permeability Production Wells," paper SPE 22785 presented at the 1991 SPE Annual Technical Conference and Exhibition, Dallas, 6–9 October.
9. Liang, J. and Seright, R.S.: "Further Investigations of Why Gels Reduce Water Permeability More Than Oil Permeability," *SPEPF* (November 1997) 225.
10. Al-Sharji, H.H. *et al.*: "Pore-Scale Study of the Flow of Oil and Water Through Polymer Gels," paper SPE 56738 presented at the 1999 SPE Annual Technical Conference and Exhibition, Houston, 3–6 October.
11. Zaitoun, A., Bertin, H., and Lasseux, D.: "Two-Phase Flow Property Modifications by Polymer Adsorption," paper SPE 39631 presented at the 1998 SPE/DOE Improved Oil Recovery Symposium, Tulsa, 19–22 April.
12. Nilsson, S., Stavland, A., and Jonsbraten, H.C.: "Mechanistic Study of Disproportionate Permeability Reduction," paper SPE 39635 presented at the 1998 SPE/DOE Improved Oil Recovery Symposium, Tulsa, 19–22 April.
13. Liang, J. and Seright, R.S.: "Wall-Effect/Gel-Droplet Model of Disproportionate Permeability Reduction," *SPEJ* (September 2001) 268.
14. White, J.L., Goddard, J.E., and Phillips, H.M.: "Use of Polymers To Control Water Production in Oil Wells," *JPT* (February 1973) 143.
15. Willhite, G.P. *et al.*: "Mechanisms Causing Disproportionate Permeability in Porous Media Treated With Chromium Acetate/HPAAM Gels," paper SPE 59345 presented at the 2000 SPE/DOE Improved Oil Recovery Symposium, Tulsa, 3–5 April.
16. Seright, R.S.: "Improved Techniques for Fluid Diversion In Oil Recovery," final report, DOE/BC/14880-15, U.S. DOE (January 1996) 97–108.
17. Dunsmuir, J.H. *et al.*: "X-Ray Microtomography: A New Tool for the Characterization of Porous Media," paper SPE 22860 presented at the 1991 SPE Annual Technical Conference and Exhibition, Dallas, 6–9 October.
18. Flannery, B.P. *et al.*: "Three-Dimensional X-Ray Microtomography," *Science* (18 September 1987) **237**, 1439.
19. Coles, M.E. *et al.*: "Developments in Synchrotron X-Ray Microtomography With Applications to Flow in Porous Media," *SPE* (August 1998) 288.
20. Zhou, M. *et al.*: "Irreducible Water Distribution in Sandstone Rock: Two Phase Flow Simulations in CT-based Pore Network," *Phys. Chem. Earth (A)* (2000) **25**, No. 2, 169.
21. Coles, M.E. *et al.*: "Pore Level Imaging of Fluid Transport Using Synchrotron X-Ray Microtomography," paper 9628 presented at the 1996 Intl. Symposium of the Soc. of Core Analysts, Montpellier, France, 8–10 September.
22. Hazlett, R.D., Chen, S.Y., and Soll, W.E.: "Wettability and Rate Effects on Immiscible Displacement: Lattice Boltzmann Simulation in Microtomographic Images of Reservoir Rocks," paper presented at the 1996 Intl. Symposium on Evaluation of Reservoir Wettability and its Effect on Oil Recovery, Montpellier, France, 11–13 September.
23. Lindquist, W.B. *et al.*: "Pore and Throat Size Distributions Measured From Synchrotron X-Ray Tomography Images of Fontainebleau Sandstones," *J. Geophys. Research* (2000) **105B**, 21508.
24. Chatzis, I., Morrow, N.R., and Lim, H.T.: "Magnitude and Detailed Structure of Residual Oil Saturation," *SPEJ* (April 1983) 311.
25. Chatzis, I., Kuntamukkula, M.S., and Morrow, N.R.: "Effect of Capillary Number on the Microstructure of Residual Oil in Strongly Water-Wet Sandstones," *SPE* (August 1988) 902.
26. Seright, R.S.: "Using Chemicals to Optimize Conformance Control in Fractured Reservoirs," annual report (DOE/BC/15110-6), Contract No. DE-AC26-98BC15110, U.S. DOE (2001) 2–39.
27. Ioannidis, M.A. *et al.*: "Comprehensive Pore Structure Characterization Using 3D Computer Reconstruction and Stochastic Modeling," paper SPE 38713 presented at the 1997 SPE Annual Technical Conference and Exhibition, San Antonio, Texas, 5–8 October.
28. Elmekies, P. *et al.*: "Further Investigations on Two-Phase Flow Property Modification by Polymers: Wettability Effects," paper SPE 64986 presented at the 2001 SPE International Symposium on Oilfield Chemistry, Houston, 13–16 February.
29. Wang, D. *et al.*: "Study of the Mechanism of Polymer Solution With Visco-Elastic Behavior Increasing Microscopic Oil Displacement Efficiency and the Forming of Steady 'Oil Thread' Flow Channels," paper SPE 68723 presented at the 2001 SPE Asia Pacific Oil and Gas Conference and Exhibition, Jakarta, 17–19 April.

---

### SI Metric Conversion Factors

bbl × 1.589 873	E-01 = m <sup>3</sup>
cp × 1.0*	E-03 = Pa·s
eV × 1.602 19	E-19 = J
ft × 3.048*	E-01 = m
°F (°F– 32)/1.8	= °C
in. × 2.54*	E+00 = cm
psi × 6.894 757	E+00 = kPa

\*Conversion factor is exact.

---

**Randy Seright** is a senior engineer at the New Mexico Petroleum Recovery Research Center at New Mexico Tech in Socorro. e-mail: randy@prcc.nmt.edu. He holds a PhD degree in chemical engineering from the U. of Wisconsin at Madison. He has served on the SPE Board of Directors and the Board Committee on Publications. **Jenn-Tai Liang** is an advisory engineer/scientist at the Idaho Natl. Engineering and Environmental Laboratory. e-mail: liang@inel.gov. Liang holds a PhD degree in petroleum engineering from the U. of Texas at Austin. He is a member of the Editorial Review Committee. **Brent Lindquist** is a professor in the Dept. of Applied Mathematics and Statistics at the State U. of New York at Stony Brook. e-mail: lindquis@ams.sunysb.edu. He holds a PhD degree in physics from Cornell. **John Dunsmuir** is a member of the technical staff in the Advanced Materials Characterization Section at Exxon Mobil Research and Engineering Corporate Strategic Research.